Title

Telencephalic outputs from the medial entorhinal cortex are copied directly to the hippocampus

Authors and Affiliations

Sau Yee Tsoi, Merve Öncül, Ella Svahn, Mark Robertson, Zuzanna Bogdanowicz, Christina McClure and Gülşen Sürmeli*

*Corresponding Author

University of Edinburgh, Centre for Discovery Brain Sciences, Edinburgh, UK

G.S., S.Y.T., M.Ö., E.S., M.R., Z.B., C.M.

Simons Initiative for the Developing Brain

G.S.

Current addresses

University College London, UK

E.S.

NHS Greater Glasgow and Clyde, UK

M.R.

VectorBuilder Inc., 1010 W 35th Street, Suite 515 Chicago, IL 60609, USA

C.M.

Abstract

Complementary actions of the neocortex and the hippocampus enable encoding and long-term storage of experience-dependent memories. Standard models for memory storage assume that sensory signals reach the hippocampus from superficial layers of the entorhinal cortex (EC). Deep layers of the EC, on the other hand, relay hippocampal outputs to telencephalic structures including many parts of the neocortex. Here we show that cells in Layer 5a of the medial EC send a copy of their telencephalic outputs back to the CA1 region of the hippocampus. Combining cell-type specific anatomical tracing, high-throughput RNA-sequencing based projection mapping and optogenetics-aided circuit mapping, we show that these projections have a unique topography and target pyramidal cells and interneurons in CA1. Our results suggest that rather than serving as a relay, deep EC may coordinate hippocampal-neocortical interactions in memory consolidation.

Introduction

Interplay between the hippocampus and the neocortex is a central tenet of theories for systems memory consolidation (Marr, 1971; McClelland et al., 1995). The entorhinal cortex (EC) mediates the two-way communication between the neocortex and the hippocampus by channelling inputs to and outputs from the hippocampus. During a new experience the superficial layers relay convergent inputs from the cortex to the hippocampus where initial conjunctive representations of our everyday experiences are generated. Subsequently during rest or sleep, hippocampal output is redistributed to the brain (Squire et al., 2015; Frankland and Bontempi 2005). Leading theoretical models consider the deep layers of EC as a relay of hippocampal output that reinstates neocortical activation patterns representing memories enabling neocortex-wide synaptic changes required for long-term storage (Koster et al., 2018; Kumaran et al., 2016; McClelland et al., 1995; Schapiro et al., 2017).

Recent discoveries revealed complex and distinct input-output interactions of molecularly defined subtypes of neurons in the deep layers of medial EC (MEC), suggesting their functions extend beyond passing on hippocampal outputs. Layers 5a (L5a) and 5b (L5b) of the EC are genetically distinct with differential input-output organisations. L5a but not L5b is the sole origin of the long-range telencephalic outputs of the EC (Sürmeli et al., 2015; Ohara et al., 2018, Kitamura et al., 2017), whereas L5b, but not L5a, is directly influenced by superficial layers of EC (Beed et al., 2020; Sürmeli et al., 2015). Inputs from the dorsal hippocampus preferentially target L5b over L5a (Rozov et al., 2020; Sürmeli et al., 2015; Wozny et al., 2018) but ventral hippocampus preferentially target L5a (Rozov et al. 2020). Moreover, the capacity of deep layers to integrate neocortical inputs with hippocampal output (Czajkowski et al. 2013; Beed et al. 2020; Sürmeli et al. 2015) suggest more complex roles.

78 An intriguing possibility, noted in experiments with classic retrograde tracers, is that deep
79 layers of MEC might also project to the hippocampal CA1 region, which provides the deep
80 EC with hippocampal output (Köhler, 1985; Witter and Amaral, 1991). Such recurrent
81 connectivity between CA1 and the deep MEC could be important in coordinating
82 hippocampal-entorhinal activity during memory consolidation (Ólafsdóttir et al. 2016),
83 provide a shortcut for hippocampal outputs to re-enter the hippocampus (Kumaran and
84 McClelland, 2012; Kloosterman et al., 2003) or have a more global coordination function
85 encompassing the hippocampus and the neocortex (Khodagholy et al., 2017). Despite its
86 potential functional significance, the key properties of this projection pathway including
87 whether it originates from a particular subset of neurons and which neurons it targets in the
88 hippocampus remain unknown.
89
90 Here we reveal that neurons in L5a, but not L5b, of the MEC project to hippocampal CA1.
91 We establish that the telencephalon-projecting neurons copy their outputs directly to
92 pyramidal and subclasses of interneuron populations. Our results suggest that Layer 5a of
93 the MEC has a dual function in coordinating neocortical and hippocampal networks.
94
95
96 **Results**
97 To find out whether neurons in either L5a or L5b project to the hippocampus we injected a
98 retrograde adeno-associated viral vector (AAV) expressing green fluorescent protein (GFP)
99 into intermediate CA1. As well as finding retrogradely-labelled cell bodies in layer 3 of MEC,
100 which contains neurons that are well-established as a critical input to stratum lacunosum of
101 CA1 (Naber et al., 2001), we also found labelled cell bodies in L5a, which we identified by
102 immunostaining against the ETS variant transcription factor-1 (Etv1) protein. Retrogradely-
103 labelled neurons were not found in L5b (Fig. 1a; Sürmeli et al., 2015).

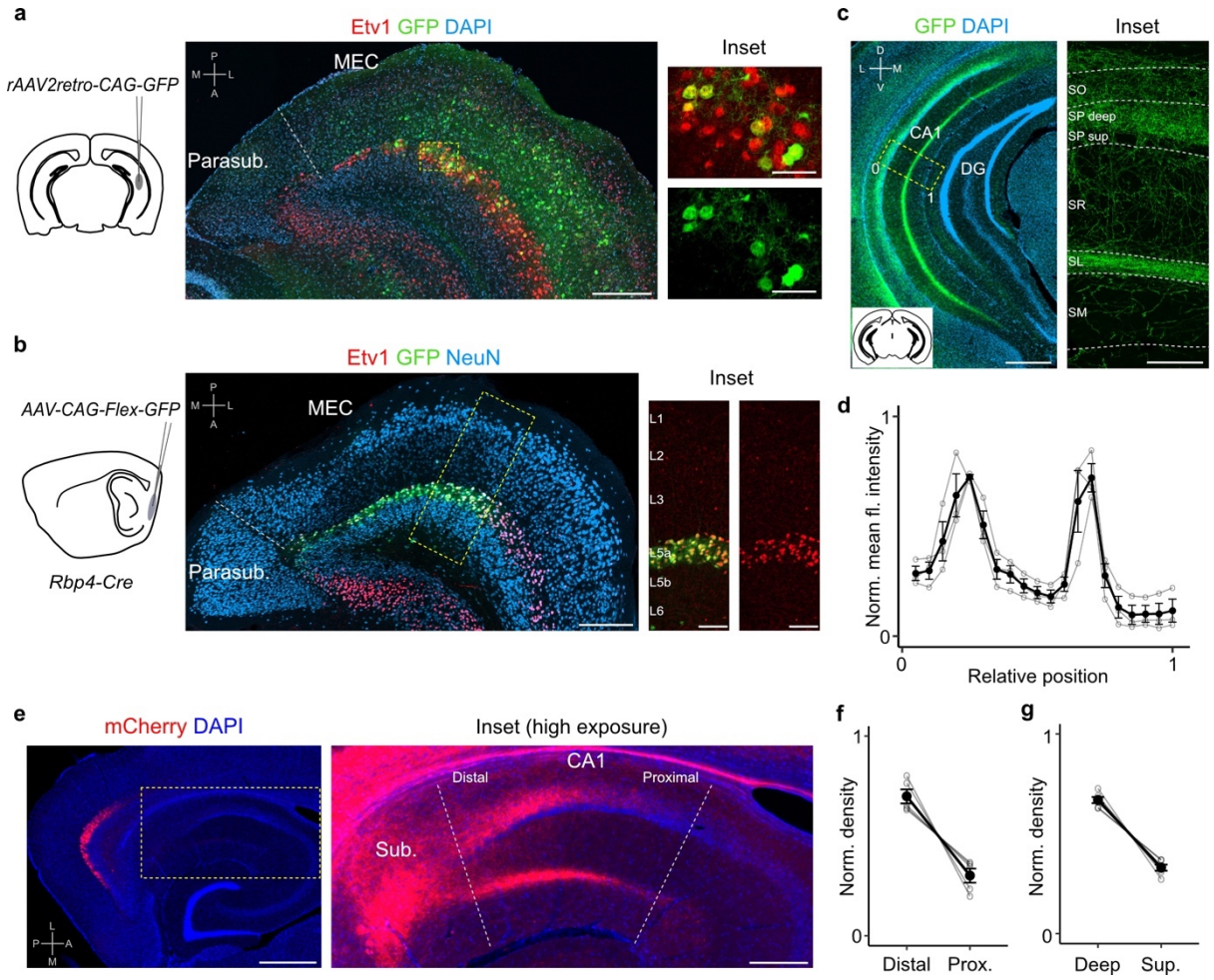

Figure 1. Origin and distinct topography of entorhinal deep layer projections to CA1
a, Left: A retrograde AAV virus was injected in the intermediate hippocampus. Middle: Entorhinal area on a horizontal brain section. Retrogradely-labelled neurons were found in L3 as well as L5a, marked by Etv1 expression (Scale bar: 250 µm). Inset: high-magnification image of boxed region in left panel showing co-expression of GFP and Etv1 (Scale bar: 50 µm).
b, Left: *Rbp4-Cre* mice were injected in the deep MEC with a Cre-dependent virus expressing GFP. Middle: expression of GFP overlaps with expression of Etv1 (88.6%, n = 3 mice, 1866 cells; Scale bar: 250 µm). Inset: high-magnification of boxed region in middle panel (Scale bar: 100µm).
c, Coronal section showing the distribution of axons of MEC L5a cells in CA1 (Scale bar: 500 µm). Inset: high-magnification image of boxed region in left panel (Scale bar: 100 µm).
d, Quantification of fluorescence intensity across the layers of CA1. The area between 0 and 1 in **c** was divided into 20 bins, and the mean fluorescence intensity was calculated for each bin. Values shown are normalised mean fluorescence intensity values (n = 6 mice, 2 sections per brain).
e. Left: Horizontal section showing the injection site at low exposure. Right: A high exposure image from the hippocampal area of the same tissue showing the distribution of L5a axons across the proximal-distal axis of CA1 (Scale bar: 250 µm).
f. Normalised mean fluorescence density values in proximal versus distal CA1 (n = 5 mice).
g. Normalised mean fluorescence density values in deep versus superficial SP (n = 6 mice). Within SP, axon density in deep SP was significantly higher than density in superficial SP (paired one-tailed Wilcoxon signed rank test, p = 0.0156, effect size = 0.899, n = 6).

104 To further investigate this projection, we identified and validated a transgenic mouse line that
105 enables specific genetic access to L5a. In this mouse line, Cre expression is driven by the
106 promoter of the retinol binding protein 4 gene (*Rbp4-Cre*; Gerfen et al., 2013). Following
107 injection of a Cre-dependent AAV expressing GFP or mCherry into the deep MEC of *Rbp4-*
108 *Cre* mice, fluorescent signal was detected mainly in L5a (Fig. 1b and Extended Data Fig.
109 1a). The majority of labelled L5a neurons expressed Etv1 (88.6%, n = 3 mice, 1866 cells;
110 Fig. 1b), similar to L5a neurons that were retrogradely labelled from the hippocampus
111 (78.8%, n = 3 mice, 749 cells) or from cortical (89.2%, n = 8 mice, 2175 cells) and
112 subcortical target areas (89.0%, n = 7 mice, 1771 cells; Extended Data Fig. 1b). Thus, like
113 telencephalon-projecting L5a neurons, deep MEC neurons that project to the hippocampus
114 are distinguished by expression of Etv1 and can be genetically accessed using *Rbp4-Cre*
115 mice.
116
117 To what extent does the projection from L5a to CA1 differ from previously-identified
118 projections arising from superficial layers of MEC? In contrast to projections from superficial
119 MEC, which target either stratum lacunosum (SL) or stratum moleculare (SM) of CA1
120 (Kitamura et al., 2014), axons from L5a neurons were primarily found in deep stratum
121 pyramidale (SP) and stratum lacunosum (SL) but were sparse in stratum moleculare (SM;
122 Fig. 1c,d,e,g). Axons from L5a also differed in their proximo-distal organisation within CA1.
123 Whereas projections from superficial layers of MEC favour proximal CA1 (Tamamaki and
124 Nojyo, 1995), axons from L5a had highest density in distal CA1 (paired one-tailed Wilcoxon
125 signed rank test, p = 0.0312, n = 5 mice; Fig. 1e,f and Extended Data Fig. 1c). We observed
126 the same topography when axon terminals were labeled using fluorescently-tagged
127 presynaptic proteins confirming that the topography is not the result of labelling of passing
128 axons (Extended Data Fig. 1d,e). This distinct topography suggests a unique functional role
129 for the projections from L5a of MEC to CA1.
130

131 Our findings suggest two intriguing possibilities for the organisation of output neurons in L5a
132 of the MEC. The hippocampus-projecting neurons in L5a may be distinct from the
133 telencephalon-projecting neurons, implying separate processing within the deep MEC layers
134 of signals to the hippocampus and telencephalon. Alternatively, the same neurons in L5a
135 may project to both the telencephalon and the hippocampus, implying that telencephalic
136 outputs from MEC are copied back to the hippocampus. To distinguish between these
137 possibilities we used a combinatorial viral labelling strategy. We restricted reporter gene
138 expression to subpopulations of L5a cells that project to specific targets by injecting a
139 retrograde AAV expressing Cre recombinase in either the retrosplenial cortex (RSC) or
140 nucleus accumbens (NucAcb), and a Cre-dependent fluorescent reporter virus into the MEC
141 (Fig. 2a,b and Extended Data Fig. 2a,b,c,d). With this approach we detected in CA1
142 fluorescently-labelled axons originating from both RSC-projecting and NucAcb-projecting
143 L5a neurons (Fig. 2c,d). The axon distribution across layers was similar to when L5a
144 neurons were labelled in bulk using the *Rbp4-Cre* mouse line (Fig. 2e,f). These results
145 establish the principle that axon projections from L5a of MEC to the hippocampus are
146 collaterals of projections to telencephalic targets. However, it is unclear from these
147 experiments whether this principle applies to projections from L5a to all of its many
148 telencephalic targets.
149
150 Entorhinal cortex outputs have diverse targets, including the entire cortical mantle as well as
151 parts of the basal ganglia and amygdala (Swanson and Köhler, 1986). To test whether axon
152 collateralisation to the hippocampus is a general feature of all telencephalon-targeting
153 neurons, we used Multiplex Analysis of Projections by Sequencing (MAPseq; Kebschull et
154 al., 2016), a high-throughput method of mapping single-neuron projections by tagging them
155 with unique RNA sequences or barcode RNAs. We injected the MAPseq barcode RNA virus
156 library into the full dorso-ventral extent of the deep MEC (Extended Data Fig. 3a) and
157 quantified barcode RNA expression in tissue collected from dorsal and ventral MEC, dorsal
158 and ventral hippocampus and three major divisions of the brain (isocortex, cerebral nuclei

159 (CNU), olfactory areas and cortical subplate (Olf/Ctxsp), (Fig 3a, see methods for detailed

160 description). The majority of barcodes that were detected in any one

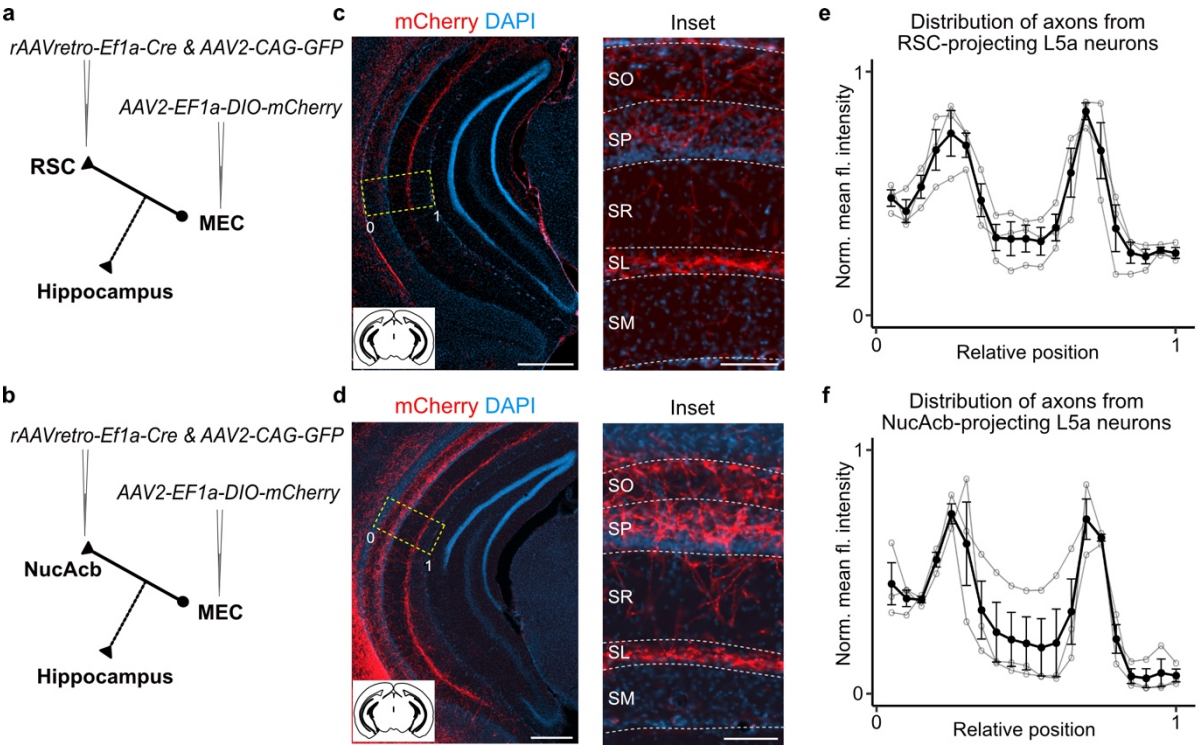

Figure 2. Retrosplenial cortex and Nucleus accumbens outputs of the MEC is copied to CA1
a, b, Experimental strategy. In wild-type mice, a retrogradely-transported virus expressing Cre was injected in either the retrosplenial cortex (RSC; **a**) or nucleus accumbens (NucAcb; **b**), while a Cre-dependent reporter virus was injected in the deep MEC.
c, d, Hippocampal axon collaterals of RSC-projecting **(c)** or NucAcb-projecting MEC neurons (**d**; Scale bar: 250 µm). Inset: high-magnification image of boxed region in left panels showing distribution of axons across CA1 layers (Scale bar: 100 µm).
e, f, Quantification of mean fluorescence intensity across the layers of CA1 when only RSC-projecting (**e**) or NucAcb-projecting (**f**) MEC neurons were labelled (n = 3 mice for each group). Axon topography is similar to when L5a neurons are marked globally in the *Rbp4-Cre* line.

161 of the three target divisions (isocortex, CNU or Olf/Ctxsp) were also detected in the

162 hippocampus, suggesting that collateral axons to the hippocampus are a common feature of

163 telencephalon-projecting neurons (Fig. 3b). The results were similar regardless of whether

164 neurons were located in dorsal or ventral MEC (Extended Data Fig. 3b), suggesting that

165 collateralisation does not depend on the neuron's position in the dorso-ventral axis of the

166 MEC. Using barcode counts as a measure of projection strength (Kebschull et al., 2016) we

167 further found that dorsal MEC neurons preferentially project to dorsal aspects of the

168 hippocampus and ventral MEC neurons to the ventral aspects, indicating that the back-
169 projections to the hippocampus are topographically organised (Fig. 3c). Together these
170 results reveal general organising principles by which all projections from MEC to the
171 telencephalon are copied back to the hippocampus.

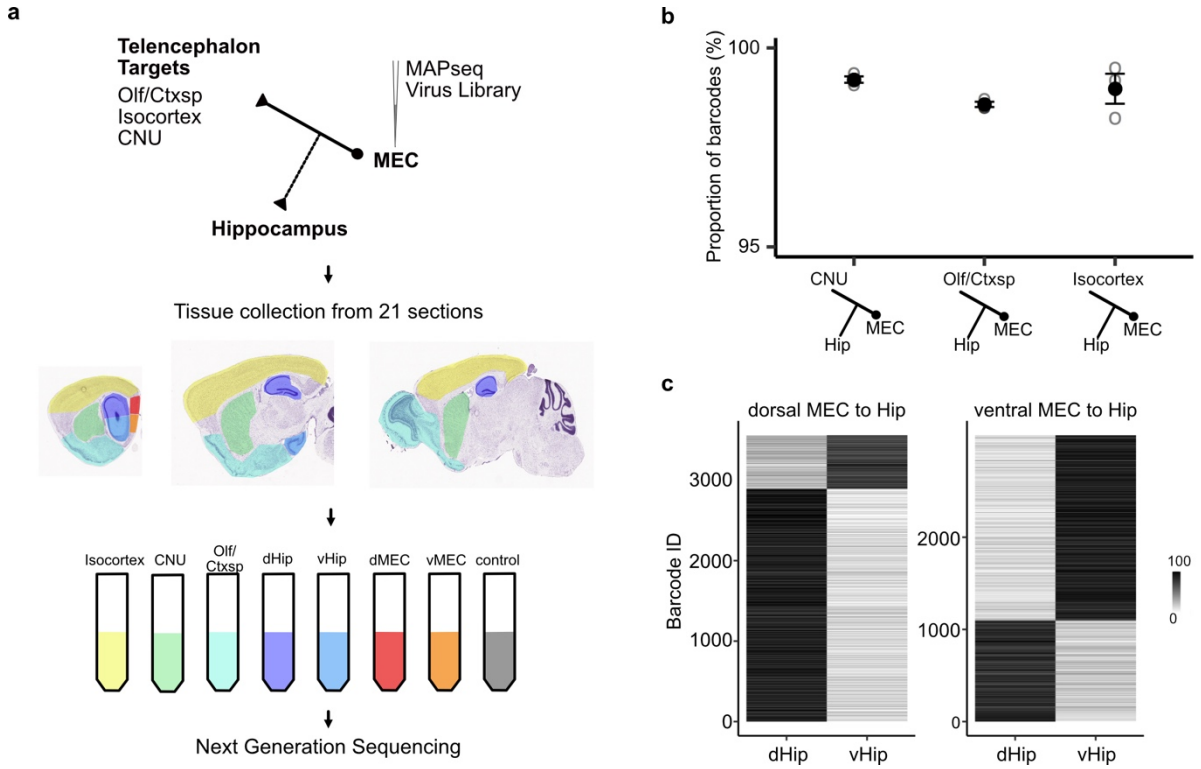

Figure 3. Telencephalic outputs are widely copied onto the hippocampus
a, Experimental strategy. A MAPseq virus library was injected into deep MEC (n = 3). 44 hrs later, mice were sacrificed and brains were sectioned sagittally at 400 µm thickness. Tissue from 5 regions (Isocortex, CNU, Olf/Ctxsp, dHip and vHip), as well as dorsal and ventral MEC were then dissected and collected in tubes. Brainstem tissue was collected as a negative control. Tissue was further processed for RNA extraction and next generation sequencing.
b, Nearly all barcodes detected in CNU, Olf/Ctxsp and Isocortex were also detected in the hippocampus (Isocortex: 98.6% ± 0.06%; CNU: 99.2% ± 0.08%; Olf/Ctxsp: 99.0% ± 0.4%; n = 3 mice, 5358 barcodes).
c, Dorso-ventral topography of projections revealed by relative barcode counts. For each barcode, counts were normalised to show the relative projection strength of each neuron to dorsal and ventral hippocampus (n = 3 mice).

172 Which cell types within the hippocampus receive signals from L5a of MEC? While the
173 compartmentalised arrangement of axons from L5a of MEC suggests selective targeting of
174 CA1 layers, axonal topography does not necessarily reflect functional connectivity.
175 Therefore, we targeted viral vectors expressing a channelrhodopsin2-mCherry conjugate

176 to L5a neurons in MEC and tested for connectivity using whole-cell ex-vivo patch clamp
177 recordings from CA1 neurons.
178
179 We focused initially on responses of pyramidal cells. Brief light pulses evoked depolarising
180 sub-threshold postsynaptic potentials (PSPs) in 64% of SP pyramidal neurons recorded at
181 their resting membrane potential (n = 64 cells, 27 mice, Fig. 4a,b,c, and Extended Data Fig.
182 4e). The response probability of neurons in distal CA1 was not significantly different than
183 neurons in proximal CA1 (Fig. 4d). The majority of PSPs (20 out of 26) maintained their
184 polarity when the membrane potential was adjusted from rest (Vm = -66.7 ± 0.6) to -50 mV,
185 indicating that they were glutamatergic. In these neurons EPSPs were maintained when
186 $GABA_A$ receptors were blocked with Gabazine, but were abolished by the AMPA receptor
187 antagonist NBQX, demonstrating that they are glutamatergic (Fig. 4e). The responses had
188 short latencies (3.04 ± 0.26 ms, n = 20 cells, 15 mice) that were relatively invariant from trial
189 to trial (Fig. 4f) and were independent of the response's position within a train of stimuli,
190 indicating that they are monosynaptic (Extended Data Fig. 4d). Consistent with this,
191 responses were sensitive to bath application of tetrodotoxin (TTX) but recoverable after
192 application of 4-Aminopyridine (4-AP; Fig. 4g; Petreanu et al., 2007). Together, these data
193 demonstrate that projections from L5a of the MEC provide glutamatergic excitatory inputs
194 directly to pyramidal neurons in proximal and distal CA1.
195
196 A smaller population of pyramidal neurons showed PSPs with characteristics of indirect
197 inhibitory connections (6 out of 26). These responses either reversed polarity when the cell
198 was held above the chloride reversal potential (Fig. 4h) or had an early depolarising and a
199 late hyperpolarising component (Extended data Fig. 4b). Application of Gabazine either
200 completely blocked the PSPs (Fig. 4i) or revealed a larger excitatory component that was
201 sensitive to application of NBQX (Extended data Fig. 4b). Thus, inputs from L5a of the MEC
202 also recruit local interneurons that provide inhibitory input to SP pyramidal neurons.

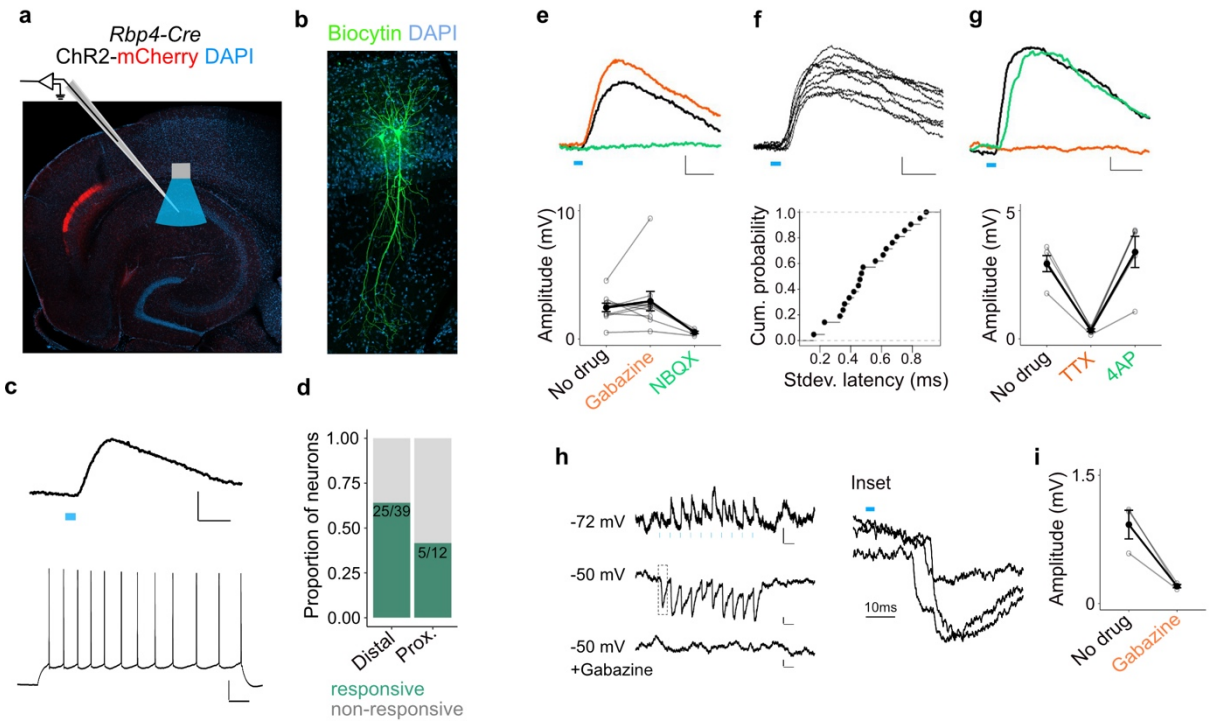

Figure 4. L5a neurons of the MEC provide direct excitatory and indirect inhibitory inputs to pyramidal cells in CA1

a, Experimental design showing viral expression, placement of patch-clamp electrode and light delivery over CA1.

b, Examples of biocytin-filled pyramidal neurons recorded in CA1.

c, Top: an example electrical recording of a pyramidal neuron at rest (-67 mV) showing depolarizing responses upon 3 ms light stimulation (top) (blue line, Scale bar: 1 mV, 10 ms). Bottom: train of action potentials upon 200pA step-current injection (bottom). (Scale bar: 20 mV, 100 ms)

d, Proportion of responsive pyramidal neurons located in the distal and proximal halves of CA1. The difference in proportions was not significant (X-squared = 1.0932, df = 1, p-value = 0.2958, Chi-squared test, n = 12 cells in proximal and n = 39 cells in distal CA1).

e, Effects of bath application of Gabazine (orange, n = 10 cells, 9 mice) and NBQX (green, n = 5 cells) on PSPs recorded from a pyramidal neuron (Scale bar: 0.5 mV, 10 ms) and a summary plot of PSP amplitude measurements for all tested pyramidal neurons. Note that some neurons were only treated with Gabazine which did not cause a significant change in amplitudes (p = 0.97, 2-tailed Student's t-test, n = 10 cells, 9 mice).

f, An example of ten consecutive PSP responses recorded from a single pyramidal neuron illustrates the short and invariant latency of PSPs (Scale bar: 0.5 mV, 10 ms) and a cumulative probability plot of standard deviation of latencies for neurons with PSP responses that were > 1 mV in amplitude (n = 20 cells).

g, Effects of bath application of TTX (orange) and 4-AP (green) on PSPs recorded from a pyramidal neuron (Scale bar: 0.5 mV, 10 ms) and a summary plot of changes in PSP amplitudes for all tested pyramidal neurons. TTX application abolished responses (n = 5 cells, 5 mice, p = 0.01, 2-tailed Student's t-test).

h. An example inhibitory PSP response recorded from a pyramidal neuron upon 10 Hz light stimulation (blue bars). Response polarity reversed when the neuron's membrane potential was adjusted to -50 mV and was abolished after application of Gabazine (Scale bars: 0.2 mV, 100 ms). Inset shows the long latency (> 10 ms) of PSP onset indicating polysynaptic connectivity.

i. Effects of bath application of Gabazine on the response amplitude of long latency PSPs (n = 3 cells).

203 To identify which interneurons in CA1 were targets of L5a projections, we tested responses
204 of interneurons in all layers. In SP we distinguished interneurons from principal cells either
205 by classifying them based on biophysical properties (fast-spiking: SP_{FS} and non-fast spiking:
206 SP_{NFS}; Extended Data Fig. 4a and see methods), or by recording from fluorescently-labelled
207 GABAergic or parvalbumin-expressing (PV+) inhibitory neurons in double transgenic mice
208 (Fig 5a,b, and Extended Data Fig. 4c). Stimulation of L5a axons elicited both sub-threshold
209 and supra-threshold responses primarily in SP, SR and SL interneurons (Fig. 5c,d and
210 Extended Data Fig. 4e). Depolarising PSPs were observed in 64% of the SP_{FS} including PV+
211 interneurons, 46% of the SP_{NFS}, 64% of SR and lower proportions of recorded neurons in SL
212 (31%), SM (23%) and SO (16%). Except for interneurons in SO, PSPs in all layers showed
213 characteristics of monosynaptic connectivity (Fig. 5g,h,i,j and Extended Data Fig. 4g,h) and
214 AMPA receptor-mediated glutamatergic synaptic transmission (Fig. 5e,f and Extended Data
215 Fig. 4f). Therefore, projections from L5a of MEC recruit CA1 interneurons through
216 monosynaptic inputs driven by excitatory glutamatergic synapses.

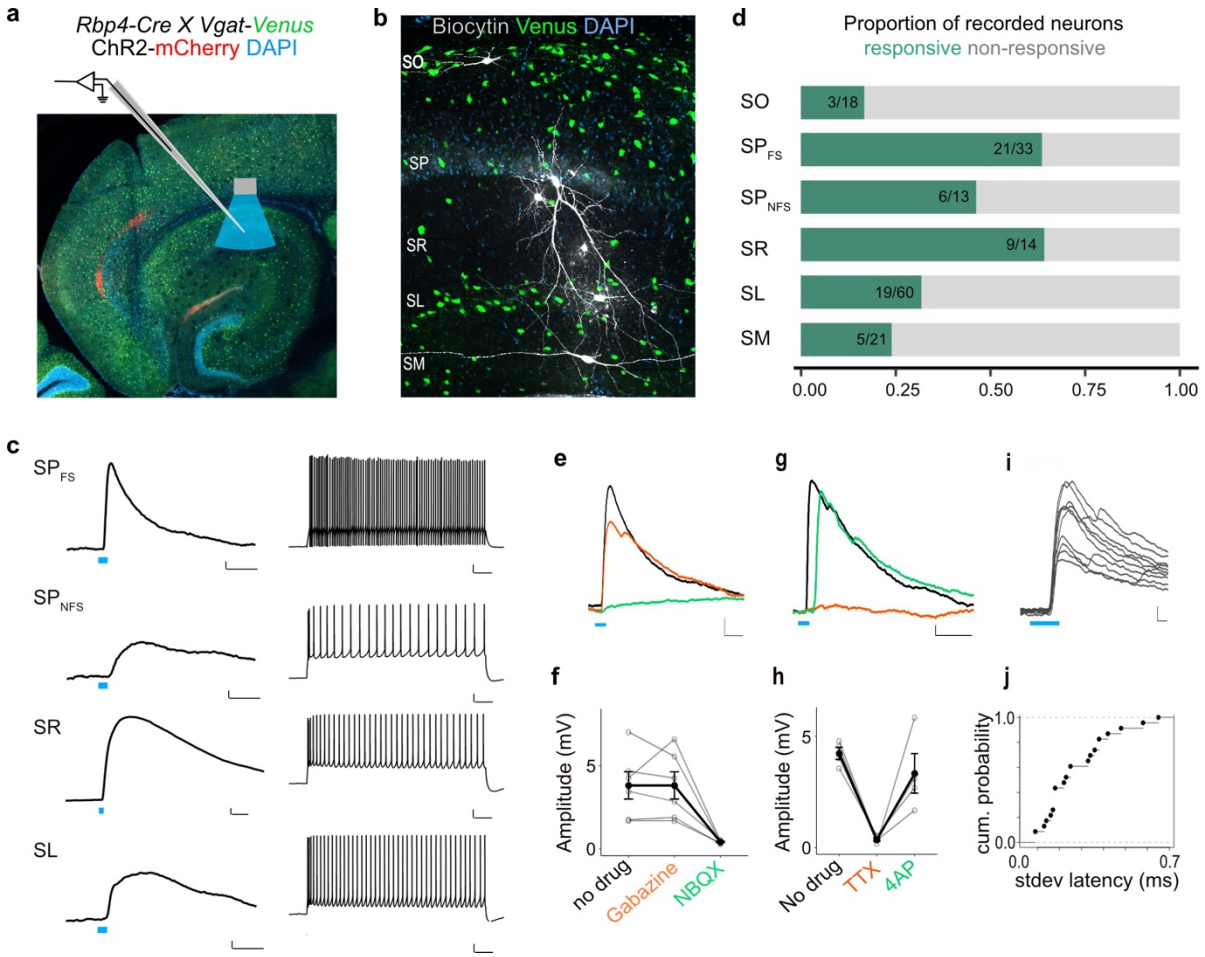

Figure 5. L5a neurons of the MEC provide direct excitatory inputs to interneurons in CA1.
a, Experimental design showing viral expression, patch pipette and light stimulation. Interneurons are marked by the expression of venus fluorescent protein driven by the vesicular GABA transporter (*Vgat*) gene's promoter.
b, Biocytin-filled neurons in the *Rbp4-Cre X Vgat-Venus* double transgenic mouse line. Fluorescent labelling facilitated patch-clamp recordings made from GABAergic interneurons and distinguishing SR, SL and SM layers.
c, Representative examples of depolarising responses recorded at resting membrane potential following 3 ms blue light stimulation (blue line) of L5a axons in CA1 (left) (Scale bar: 1 mV, 10 ms). Neurons in SO and SM were typically not responsive (< 30%). Responses from SR neurons were on average larger than the responses from neurons in other layers (Scale bar: 1 mV, 10 ms). Neurons' spiking response to injecting 200 pA current (right) (Scale bar: 10 mV, 100 ms).
d, Proportion of responsive interneurons in all layers of CA1 recorded at resting membrane potential. Green highlighted segment corresponds to the proportion of cells with depolarising membrane potentials; grey highlighted segment corresponds to neurons with no change in their membrane potential.
SO: n = 18 cells, 10 mice;
SP_{FSint} : n = 33 cells, 8 *Rbp4-Cre X Pvalb-Flp mice*, 5 *Rbp4-Cre X Vgat-Venus mice*, 8 *Rbp4-Cre* mice;
SP_{NSFint}: n = 13 cells, 11 *Rbp4-Cre* mice, 1 *Rbp4-Cre X Vgat-Venus* mouse;
SR: n = 14 cells, 6 mice; SL: n = 60 cells, 15 mice; SM: n = 21 cells, 10 mice
e, f, Effects of bath application of Gabazine (orange) and NBQX (green) on PSPs recorded from a fast-spiking pyramidal layer interneuron (left) (Scale bar: 1 mV, 5 ms)**.** Summary quantification of PSP amplitudes for multiple cells (right). The PSP amplitudes were largely unaffected by application of Gabazine (SP_{int} : n = 6 cells, p = 0.99 2-tailed Student's t test) but were largely blocked by NBQX (SP_{int} : n = 5 cells, p = 0.03, 2-tailed Student's t test) indicating AMPA receptor-mediated glutamatergic synaptic transmission.
g, h, Effects of bath application of TTX (orange) and 4-AP (green) on the response amplitude PSPs recorded from pyramidal layer interneurons. Example traces from a fast-spiking pyramidal layer interneuron (Scale bar: 1 mV, 5 ms). Summary plots of response amplitude measurements from multiple recordings (SP_{int}: n = 4 cells).
i, j, An example of ten consecutive PSP responses recorded from a single fast-spiking interneuron in SP illustrates the short and invariant latency of PSPs. Cumulative probability plots of standard deviation of latencies for neurons with PSP responses that were > 1 mV in amplitude (mean latency SP: 2.08 ± 0.08 ms, n = 21 cells).

Discussion

Together our results suggest a substantial revision to the idea that the entorhinal deep layers unidirectionally convey hippocampal output messages to the neocortex. Using two lines of evidence, combinatorial viral labelling and MAPseq, we show that L5a axons bifurcate to target both the telencephalon and the hippocampus. Our data shows that nearly all telencephalic output is copied back to the hippocampus regardless of its destination in the telencephalon following distinct topographical organization rules.

Although cells in deep entorhinal layers have been previously observed when retrograde dyes were placed at the CA1-subiculum border (Köhler, 1985; Witter and Amaral, 1991) the tools we have introduced in this study made it possible to investigate the distinct source of these projections and their targets within CA1. Our observation that L5b does not participate in this pathway reinforces the complex input-output organisation of the deep MEC. L5b is an integrator of local and neocortical input with hippocampal output and distributes its signals locally within MEC. It provides an indirect feedback message to the hippocampus via its projections to L3 of the MEC. L5a on the other hand appears not to be a focus of local computations. Instead, it is suited to coordinate the wider hippocampal-neocortical loop by providing a rapid copy of entorhinal output onto CA1.

In understanding the respective roles of projections from the superficial versus deep EC to CA1, elucidating the topographical organization of the two projection pathways is crucial. Our results show that in the transverse axis of CA1, the density of projections originating from L5a of the MEC has a gradient descending towards proximal CA1 (towards CA2). This is in contrast to previous reports where traditional (non-cell type specific) tracers targeted to MEC revealed dense projections in proximal but not in distal CA1 (Tamamaki and Nojyo, 1995; Naber et al., 2001). The topographical organization of projections originating specifically in L5a of the MEC that we reveal here suggests that this pathway serves a

function that is distinct from the ones that originate in the superficial layers of MEC instead of merely supplementing them (Witter et al., 2017). It also opens up a possibility for the lateral and medial entorhinal cortex input streams to converge in CA1.

Our high-throughput sequencing based projection mapping approach allowed us to also reveal the topography of the deep layer projections to the hippocampus in the dorso-ventral axis. The dorso-ventral target zone in the hippocampus of axons originating from L5a of the MEC is in register with the dorso-ventral position of the originator cells in L5a. This is similar to the topography of perforant-path projections of the superficial EC targeting the dentate gyrus supporting the view that dorso-ventral compartments of the hippocampus might operate independently (Ruth et al., 1982; Dolorfo and Amaral 1998).

Our findings raise new questions about the functional roles of outputs from the entorhinal cortex, and about the nature of interactions between the entorhinal cortex and the hippocampus. Telencephalic projections of L5a cells have been shown to be necessary for long-term memory formation and retrieval (Kitamura et al., 2017) likely by distributing compressed hippocampal outputs to the neocortex (McClelland et al., 1995). Returning a copy of these outputs back to CA1 might create a self-reinforcing or a self-correcting loop. They might also provide a gating signal to modulate the impact in CA1 of inputs from CA3 (Dudman et al., 2007) and/or neocortical return inputs via L3 of EC. It is also conceivable that they influence mechanisms of learning and memory by affecting rhythmic network activity through the inputs on the pyramidal cells and interneuron populations that we described here (Colgin 2016; Ognjanovski et al. 2017; Xia et al. 2017). In addition, L5a might also relay cortical input directly to CA1 however sources of cortical afferents to entorhinal L5a remain to be established.

Methods

Mice

All animal experiments were approved by the University of Edinburgh animal welfare committee and were performed under a UK Home Office project license. The *Rbp4-Cre* mouse line was generated by GenSat and obtained from MMRRC (*Tg(Rbp4-cre)KL100Gsat/Mmucd*). The *Vgat-Venus* mouse line was generated by Dr. Atsushi Miyawaki at RIKEN, Wako, Japan(Wang et al., 2009). The *Pvalb-Flp* mouse line was obtained from Jackson Laboratories *(B6.Cg-Pvalb-tm4.1(FlPo)Hze/J; Jax 022730)*. Wild-type mice were obtained from Charles River Laboratories C57Bl6J stock. Double transgenics were generated by crossing the *Rbp4-Cre* line to the *Vgat-Venus* or the *Pvalb-Flp* lines. *Rbp4-Cre* and *Pvalb-Flp* lines were maintained as heterozygous and all mice were on C57Bl6 background.

Viral constructs and injection strategy

8 to 14 week-old male and female mice were used in all experiments. For targeting deep MEC a craniotomy was made 3.4 to 3.65 mm lateral to the bregma (X) between the transverse sinus and lambdoid suture (Y = 4.5 to 5 mm caudal to bregma). The injection pipette was at a 9 degree angle caudal to the dorsoventral plane (See Fig. 1b). 100 nl of virus was slowly released at four Z-depths 3.0, 2.8, 2.6 and 2.4 mm from the surface of the brain. 3 mins after delivering the virus the injection needle was retracted to the next injection depth until the most dorsal location where 10 mins past before the needle was fully retracted. For anterograde tracing of L5a axons and terminals *AAV-EF1a-DIO-mCherry* (serotypes 2 and 5, titer 5.3 x 10^{12}, lot #AV4375H, K., Deisseroth, UNC Vector Core), *AAV-CAG-FLEX-GFP* (titer 3.7 x 10^{12}, lot #AV4530B, E. Boyden, UNC Vector Core) and AAV-hSyn-FLEx-mGFP-2A-Synaptophysin-mRuby (Addgene:71760) were used.

294 For injections in CA1 a craniotomy was made 3.5 mm lateral and 3.30 mm caudal to the
295 bregma in C57BL6J mice. 100nl virus was delivered at 3.0, 2.8, 2.6, 2.4 and 2.2 mm from
296 the surface. For retrograde labelling of hippocampus-projecting EC neurons, 100nl of a
297 *rAAV2retro-CAG-GFP* (titre 4.3 x 10^{12}, lot #AV6951B, E. Boyden, UNC Vector Core) was
298 injected at each depth.

299 To assess whether telencephalic projection neurons in L5a of MEC co-express Etv1
300 (Extended Data Fig. 1b), fluorophore coupled choleratoxin beta subunit (CTB-Alexa 488 and
301 CTB-Alexa 555) was injected at various sites in wild-type C57BL6J mice as previously
302 described(Sürmeli et al., 2015).

303 To achieve Cre expression in target specific subpopulation of L5a neurons in the MEC (Fig.
304 2) a *rAAVretro-EF1a-Cre-WPRE* (viral construct was a gift from Karl Deisseroth, titre 2.4 x
305 10^{12}) was made using an AAV-retro helper plasmid (Addgene plasmid ID 81070) as
306 described previously(McClure et al., 2011). A cocktail of *rAAVretro-EF1a-Cre-WPRE* and
307 *AAV-CAG-GFP* (titer 4.3 x 10^{12}, lot #AV6951B, Boyden, UNC Vector Core) viruses were
308 injected either in NucAcb (X: +1.0 mm; Y: +1.2 mm; Z: -3.8, -4.0 mm) or RSC (X: +0.4 mm;
309 Y: -2.8, -3.2 mm; Z: -0.9 mm) in wild-type mice. A Cre inducible reporter virus was also
310 injected in the MEC as described above. GFP expression driven by the *CAG* promoter at the
311 target site was used for verification of injection location.

312 To achieve expression of channelrhodopsin-2 in L5a axons, we injected *AAV2-EF1a-DIO-*
313 *hChR2(H134R)-mCherry-WPRE-pA* (titer 5.1 x 10^{12}, lot #AV4319J, Deisseroth) in the MEC
314 of the *Rbp4-Cre* or the *Rbp4-Cre X Vgat-Venus* or the *Rbp4-Cre X Pvalb-FLP* double
315 transgenic mice. Additionally, in order to fluorescently label parvalbumin expressing
316 interneurons in CA1 a Flp recombinase-dependent AAV vector was constructed in house
317 and injected in the hippocampus (X: +3.0 mm; Y: -3.5 mm; Z: -2.0, -3.0 mm, 200 nl virus was
318 injected at each Z-depth). To produce the virus, the viral construct pAM-FLEX-GFP(Murray
319 et al., 2011) (a gift from Peer Wulff) was used as the viral backbone. The eGFP, loxP and

320 lox2272 sites were removed and replaced with a synthesised cassette (GenScript)
321 containing a multiple cloning site flanked by two sets of heterotypic (FRT and F3),
322 antiparallel FRT sites to produce pAM FLPX. For pAM FLPX eGFP and pAM FLPX mCherry,
323 the fluorescent proteins were amplified from pAM FLEX eGFP and pmCherry-C1 (Clontech)
324 respectively, with EcoRI and SacI overhangs and cloned into pAM FLPX. All AAV preps
325 were generated in house as previously described(McClure et al., 2011) and were titered by
326 qPCR following expression in HEK cells (> 10^{12} genome copies (GC)/ml).

327 Tissue processing and immunohistochemistry

328 3 to 4 weeks after the virus injection surgery, mice were transcardially perfused with 4%
329 paraformaldehyde as previously described(Sürmeli et al., 2015). Brains were sectioned at 60
330 µm using a cryostat (Leica CM3050 S) either coronally or horizontally and sections were
331 stored in PBS at 4°C. All subsequent incubation and washing steps were carried out at 4°C.
332 Prior to antibody staining, sections were blocked with either 5% normal goat serum (NGS;
333 Abcam: ab13970) or 2% bovine serum albumin (BSA; Sigma: A9418) in 0.3% PBST (PBS
334 with 0.3% Triton-X100) for 2hrs. Sections were then transferred to primary antibody solutions
335 made with either 5% NGS or 2% BSA in 0.3% PBST and incubated overnight. After 3
336 washes, each 20 min, in 0.3% PBST, sections were transferred to secondary antibody
337 solutions made with 0.3% PBST and, if required, NeuroTrace 640/660 (1:800; Life
338 Technologies: N21483) and incubated overnight. After 3 washes, sections were incubated in
339 DAPI (1:2,000; Sigma Aldrich: D9542) solution made in PBS for 20 min at room temperature,
340 where required, and then mounted on microscope slides using Mowiol® 4-88 (Aldrich:
341 81381). Slides were covered with glass coverslips and left to dry overnight at 4°C in the dark.
342 The following primary antibodies were used: rat anti-mCherry (1:2,000; ThermoFisher:
343 M11217), chicken anti-GFP (1:10,000; Abcam: ab13970), rabbit anti-Etv1(Arber et al., 2000)
344 (1:1,000), chicken anti-NeuN (1:1,000; Sigma Aldrich: ABN91). The following secondary
345 antibodies from Thermo Fisher Scientific were used at a concentration of 1:800: goat anti-

346 rabbit A488 (A11034), goat anti-chicken A488 (A11039), goat anti-rat A555 (A21434) and
347 goat anti-rabbit (A21244).

348 Cell counting

349 Every 4th brain section was imaged as a Z-stack (1 µm step size) using either the Zeiss
350 LSM 800 (Zen, v2.6.76) or Leica SP8 confocal microscope (Leica Application Suite X,
351 v3.5.6.21594) at 20x magnification. Regions of interest were drawn around L5a and cell
352 counting was carried out either manually using Fiji software, or using cell-counting tools in
353 Vision4D (Arivis, v3.2.0).
354
355 The boundaries for L5a were determined using either a DAPI or Neurotrace counterstain.
356 The border between medial and lateral divisions of EC was determined in each section using
357 layer 2 as a guide – in lateral EC, layer 2 is separated into two distinct layers, while this
358 separation is not seen in medial EC(Cappaert et al., 2015).

359 Quantification of the distribution of fluorescent signal

360 *Quantification of fluorescence across the radial axis of the CA1*

361 The distribution of axons of L5a neurons in the radial axis of the hippocampal CA1 was
362 quantified in slide-scanner images (Fig. 1) or confocal images (Fig. 2) using Fiji software.
363 Coronal brain sections between 3.28 to 3.58 mm posterior to Bregma, which contain distal
364 CA1, were selected for analysis. 2 sections from each brain in which the fluorescent labeling
365 was representative of all the sections were used. DAPI was used as a counterstain. In each
366 section, a 400 µm-wide rectangular ROI was drawn across the radial axes, covering all
367 layers of a randomly selected region in intermediate CA1 (Fig. 1c). This ROI was then
368 divided into 20 equal bins and the mean fluorescence intensity was calculated for each bin.

369 The mean intensity values were then normalised in each brain by scaling the values such
370 that the highest value is 1.

371 *Quantification of fluorescence in the transverse axis of the CA1*

372 A Zeiss Axioscan slidescanner was used to image every second brain section at 10x
373 magnification. The projection strengths of MEC L5a neurons to proximal and distal halves of
374 CA1 were quantified in horizontal sections located at depths between 2.56 mm to 4.12 mm
375 from the surface of the brain, with injection sites located across medial, mid and lateral MEC
376 (15-18 brain sections per mouse, n = 5 mice). GFP and mCherry fluorescence signals were
377 amplified with immunostaining as described previously. The borders of CA1 were drawn on
378 brain section images using a customisable digital microscopy analysis platform (Visiopharm),
379 and the proximo-distal border was defined as the border equidistant from the proximal and
380 distal ends of CA1. The mean fluorescence density, defined as the total number of pixels
381 above a set threshold in an area divided by the total number of pixels in the area, was
382 measured in proximal and distal CA1. The threshold was determined manually by ensuring
383 that only pixels representing axons were detected as signal. A median unsharp background
384 correction was used to remove background noise from axons outside of the focus plane of
385 the image. The mean fluorescence density values were then normalised within each brain by
386 scaling the values such that the total fluorescence density value (proximal + distal) in each
387 brain is equal to 1.

388 The spread of viral expression in MEC was assessed from the fluorescent signal in all
389 sections for each brain. Brains in which labelled neurons were found outside L5 were
390 excluded; this was a result of occasional and sparse labelling in L2 or L3 or the
391 parasubiculum in the *Rbp4-Cre* line.

392 MAPseq

393 5 C57Bl6J adult male and female mice were injected in the deep MEC with the MAPseq
394 Sindbis viral barcode library (3 x 10^{10} GC/ml) provided by the MAPseq facility (Cold Spring
395 Harbor Laboratories). To cover the whole mediolateral and dorsoventral extent of the MEC
396 virus was injected in two locations: 3.4 mm and 3.6 mm lateral to bregma. 100 nl virus was
397 delivered to 3.0, 2.8, 2.6, 2.4 mm below the surface of the brain. After 44 hrs, mice were
398 sacrificed, brains were extracted and immediately immersed in oxygenated cold ACSF
399 prepared in ultrapure water. All surgical tools and surfaces were treated with RNaseZAP
400 (Invitrogen) prior to the start of the experiment and in-between samples. 400 µm fresh
401 sagittal brain sections were cut using a vibratome(Pastoll et al., 2012). Immediately after
402 this, GFP expression in the deep EC was verified under a fluorescent microscope and tissue
403 was dissected in cold oxygenated ACSF using microdissection blades on sylgard covered
404 petri dishes which were kept on ice. Each slice was dissected on a previously unused
405 surface of the plate with fresh ACSF and a dedicated microblade was used for the dissection
406 of each brain division to prevent contamination. Tissue pieces were collected into bead
407 containing (Qiagen 69989) collection tubes (Qiagen 19560) on dry ice. After tissue
408 collection, 400 µl Trizol (Thermo Fisher Scientific #15596026) was added to each collection
409 tube. The procedure was repeated for all 5 brains. 3 brains with the largest coverage of MEC
410 deep layers were selected to proceed to the next steps. Tissue was stored at -80 degrees
411 before it was shipped on dry ice to CSHL MAPseq core facility for further processing. RNA
412 extraction, production of double stranded cDNA, library preparation and Illumina sequencing
413 and preprocessing of sequencing data was performed by the MAPseq core facility as
414 described in(Kebschull et al., 2016).

415 For the tissue dissections, identification of brain areas was done by using Allen Brain
416 Reference Atlas (https://mouse.brain-map.org/). The isocortex division included the
417 somatosensory, motor, visual, posterior parietal, anterior cingulate and retrosplenial areas
418 combined. The cerebral nuclei (CNU) division was restricted to striatum. The
419 olfactory/cortical subplate division (Olf/Ctxsp) was a combination of olfactory areas and

420 cortical subplate including amygdalar nuclei. The remaining two divisions were dorsal (dHip)
421 and ventral hippocampus (vHip) including subiculum. Some brain areas were excluded from
422 the study because of the difficulty in dissecting or identifying brain areas in the sagittal plane.
423 All sections > 3.7 mm lateral to bregma which are not annotated in Allen Brain Reference
424 Atlas were excluded. Therefore, neocortical areas in the most lateral sections such as
425 perirhinal cortex, ectorhinal cortex, temporal association areas were not included in the
426 study. The claustrum and adjacent neocortical areas (visceral, agranular insular, gustatory)
427 were excluded as it was not possible to separate these areas precisely to prevent
428 contamination between the assigned divisions. Since borders between the brain divisions
429 CNU and OLF/Ctxsp were not always clear, dissections avoided these areas hence the brain
430 areas in these divisions are partially included. White matter between the hippocampus and
431 the neocortex carrying axon tracts were also excluded. Brainstem and cervical spinal cord
432 tissue were used as control. When L5a neurons in the MEC were labelled using strategies
433 explained in Fig. 1, no axonal projections to these areas were observed (unpublished
434 experiments). Consistent with this, a low number of barcodes were identified in the negative
435 control samples (on average 1.0% of barcodes had counts in control areas, n = 3).

436 A limitation of the barcode-based single-cell tracing method comes from the possibility of
437 multiple neurons being represented by the same barcode. This is prevented by adjusting the
438 barcode diversity and the size of the target population as explained in detail in(Kebschull et
439 al., 2016). In order to assess the expected fraction of uniquely labelled neurons in our study
440 we counted the total number of neurons in L5a of the MEC. A total of 2314 ± 131, (n = 2
441 mice) NeuN-labelled neurons were counted. Using the formula $F = (1-(1/N))^{k-1}$ where N is
442 the barcode diversity (2×10^6)(Kebschull et al., 2016) and k is the number of infected
443 neurons the predicted ratio of uniquely labelled neurons is 99.9%. Multiple representation of
444 neurons due to a neuron being infected by several different barcode RNA-expressing viral
445 particles was not corrected for since the projection patterns are not affected by
446 overrepresentation of neurons(Kebschull et al., 2016).

447 *MAPseq data analysis*

448 Barcode counts were first normalised in each area by the relative number of spike-in RNAs
449 for each sample. Orphan barcodes, barcodes which did not have counts in the injection site,
450 (dMEC or vMEC) were removed. We then calculated the 95th percentile of the barcode
451 counts in our negative controls and based on this set all barcode counts of 1 to 0. A small
452 number of barcodes had a higher count in any target area compared to the injection site
453 which might be a result of incomplete dissection of the injection site or viral expression in
454 areas that the virus spilled into as we retracted the pipette. These barcodes were removed.
455 Since our goal was to find whether neurons projecting to the telencephalon also project to
456 the hippocampus we removed the barcodes that had no counts in any of the telencephalic
457 target areas. For the same reason, barcodes that were detected only in the dHip or vHip
458 hippocampus were also removed. Finally, we excluded all barcodes with counts of less than
459 400 in the injection site to minimise the possibility of incomplete transport of RNA barcodes
460 to axons in target areas due to weak expression at the cell bodies or low counts due to PCR
461 or polymerase errors. Barcodes with low counts in all target areas (< 10) were also excluded
462 to account for potential false positives.

463

464 To quantify the proportion of barcodes that were present in both a target division (Fig. 2h;
465 Isocortex, CNU or Olf/Ctxsp) and the hippocampus, the following formula was used: (total
466 number of barcodes with counts detected in both hippocampus and target division / total
467 number of barcodes with counts detected in target division). To compare the difference
468 between barcodes with the injection site in dMEC vs vMEC, the barcodes were divided into
469 two groups – “dorsal MEC”, where counts in dMEC were higher than in vMEC, and vice
470 versa for “ventral MEC”. A paired two-tailed Wilcoxon signed rank test was used to check if
471 there was a significant difference between the proportion of collateralising neurons in dMEC
472 and vMEC.

473

474 To visualise the distribution of barcode counts in dHip and vHip from “dorsal MEC” or
475 “ventral MEC” groups, we generated heat maps showing normalised projection strengths
476 between dHip and vHip for all barcodes. The normalised projection strengths were
477 calculated by the formula: projection $strength_{dHip}$ = ($counts_{dHip}$) / ($counts_{dHip+vHip}$) * 100, and
478 likewise for vHip. Barcodes were sorted by maximum projection site.
479

480 Ex-vivo electrophysiology

481 *Slice preparation*

482 Slice preparation and subsequent data acquisition was done as previously
483 described(Sürmeli et al., 2015). 3 to 4 weeks after the injection of the viral vectors ex-vivo
484 brain slices were prepared. Following decapitation, brains were immersed for 2 mins in 4°C
485 artificial cerebrospinal fluid (ACSF) of the following composition (mM): 86 NaCl, 1.2
486 NaH_2PO_4, 2.5 KCl, 25 $NaHCO_3$, 25 Glucose, 75 Sucrose, 0.5 $CaCl_2$, 7 $MgCl_2$, bubbled with
487 95% O_2 / 5% CO_2. They were then sectioned horizontally (400 µm) using a vibratome (Leica
488 VT1200) ACSF. Tissue was collected and maintained in extracellular solution of the
489 following composition (mM): 124 NaCl, 1.2 NaH_2PO_4, 2.5 KCl, 25 $NaHCO_3$, 20 Glucose, 2
490 $CaCl_2$ and 1 $MgCl_2$, continuously supplied with 95% O_2 / 5% CO_2. Slices were allowed to rest
491 for 15 mins at 35°C followed by a minimum of 30 mins recovery time at room temperature
492 before the start of the experiment.

493 *Electrophysiological recordings*

494 Whole-cell patch-clamp recordings were made in pyramidal neurons and interneurons in all
495 layers of hippocampal CA1. Typically, 2 to 3 slices from the intermediate hippocampus were
496 used where morphologies of the pyramidal cells and interneurons were confirmed to be
497 intact with post hoc staining and imaging of biocytin filled neurons. Data was collected using
498 AxoGraph (v1.7.6) software.

499 Pipettes with 4 to 6 MΩ resistance were pulled from borosilicate glass (Sutter Instruments)
500 and filled with an intracellular solution of following composition (mM): 130 K Gluconate, 10
501 KCl, 10 HEPES, 2 $MgCl_2$, 0.1 EGTA, 2 Na_2ATP, 0.3 Na_2GTP, 10 NaPhosphocreatine, 5.4
502 Biocytin. The intracellular solution was adjusted to a pH of 7.2 to 7.4 with KOH and
503 osmolarity 290-300 mOsm. All recordings were made in current clamp mode with pipette
504 capacitance neutralisation and bridge balance applied. Subthreshold membrane properties
505 were measured from the changes in membrane potential upon depolarising and
506 hyperpolarising current injections (typically -40 pA to +40 pA, in 20 pA). Rheobase was
507 established from responses to a depolarizing current ramp (50 pA/sec, maximum current
508 400 pA).

509 For optogenetic stimulation of ChR2, an LED of wavelength 470 nm (ThorLabs) was
510 attached to the epifluorescence port of the microscope. Where necessary, the irradiance of
511 the LED (max 9 mW) was controlled by voltage commands. Pharmacological tests were
512 done by bath application of the following reagents with the indicated final concentrations in
513 standard extracellular solution: Gabazine (10 μM, Hello Bio, Cat. No. HB0901), NBQX (10
514 μM, Tocris, Cat. No. 0373), D-AP5 (50 μM, Tocris, Cat. No. 0106), 4-AP (200 μM, Tocris,
515 Cat. No. 0940), TTX (1 μM, Hello Bio). To allow for morphological reconstructions cells were
516 filled with Biocytin (5.4 mM in intracellular solution, Sigma, Cat. No. B4261) during
517 electrophysiological recordings.

518 *Analysis of electrophysiological recordings*

519 Electrophysiological properties were analysed using built-in and custom routines in
520 IGORpro8 (WaveMetrics) and Matlab (MathWorks). All basic properties were established
521 from the I-V protocol described above. Input resistance was determined from the largest
522 depolarising current step injected. Sag ratio was calculated as $V_{steady\ state}$/ V_{min} from the largest
523 hyperpolarising current step. Rheobase and action potential (AP) threshold were determined
524 from the first AP during injection of steadily increasing current in a ramp. From the same

525 protocol, after-hyperpolarisation (AHP) was calculated as the difference between AP
526 threshold and the most negative peak of the hyperpolarisation following the first spike. Half-
527 width was measured as the width of the AP at half its maximum spike amplitude. Firing
528 frequency was measured from a 1 s current injection of 200 pA. Maximum firing frequency
529 was measured between the first two APs, and base frequency between the last two APs in a
530 train.

531 For optogenetic stimulations, responsiveness was confirmed for each cell by a significant
532 difference between the detected peak of change in membrane potential after light stimulation
533 and the average baseline using a 2-tailed, type 1 student's t-test. The PSP amplitude and
534 latency were measured using the Neuromatic toolbox in IGORPro8.

535 Cell types were determined based on biophysical properties extracted from
536 electrophysiology data. Pyramidal cells were identified from a max firing frequency of < 50
537 Hz, AHP < 10 mV, AP half-width ≥ 0.7 ms and sag ≤ 0.9, with descending hierarchical order.
538 Fast spiking interneurons were categorised from a max firing frequency ≥ 100 Hz, AHP ≥ 12
539 mV, AP half-width < 0.5 ms and sag > 0.9. Non-fast spiking interneurons were classified
540 from a max firing frequency 50-100 Hz, AHP ≥ 12 mV, AP half-width 0.5 to 0.9 ms, sag ratio
541 > 0.9. and max firing frequency 50-100 Hz.

542 Neurons with a resting membrane potential less negative than -50 mV or a bridge balance
543 higher than 40 MΩ were excluded from the analysis, as were neurons that did not fit within a
544 class from above criteria.

545 *Immunostaining of electrophysiology slices*

546 For identification of cells following recordings, tissue was fixed in 4% PFA overnight at 4◦C.
547 Slices were washed with PBS three times, 20 min each, and incubated in Streptavidin-Alexa
548 488 (S11223) or Alexa 647 (1:500, S32357, Invitrogen) and DAPI (1:1000, in 0.3% PBST)
549 overnight at 4°C. Slices were washed in 0.3% PBST four times and mounted on glass slides

550 with Mowiol® 4-88. Mcherry fluorescence in the MEC was examined with confocal imaging
551 and those animals where virus injection missed MEC L5 were excluded.

552 For staining of the interneuron marker parvalbumin (PV), slices were prepared as described
553 above, then incubated in primary antibody solution containing mouse anti-PV (1:1000, PV
554 235, Swant) and 5% NGS in 0.3% PBST for 48 hrs at 4°C. Slices were then washed and
555 incubated in secondary antibody solution with Alexa-conjugated Streptavidin and DAPI
556 prepared in 0.3% PBST and mounted on glass slides after overnight incubation.

557 A Zeiss LSM800 microscope was used for image acquisition of the slices. Pinhole was set to
558 1 Airy Unit. Objectives used include x10 (air), x20 (air) and x40 (oil) to image the
559 hippocampal formation, morphology of biocytin filled cells, and immunolabelling of
560 interneurons, respectively.

561 Statistics

562 Statistical tests (Student's t-test, Chi-squared test, Wilcoxon signed rank test) were
563 performed using R (www.r-project.org) 3.6.0, 4.0.0 and 4.0.3. Normality was tested for using
564 both the Shapiro-Wilk test and QQ plots. All data is presented in the format of mean ± SEM
565 unless otherwise stated. A p-value < 0.05 was regarded as significant.

566 Data availability

567 On publication data and analysis scripts will be made publicly available via University of
568 Edinburgh's Datashare service (http://datashare.is.ed.ac.uk/). This is an online data
569 repository maintained by the University. MAPseq data will be made available at NLM
570 Sequence Read Archive BioProject.

571 Code availability

Analysis script will be made publicly available upon publication via University of Edinburgh's Datashare service

Acknowledgements

We thank Matt Nolan and Nolan Lab for discussions and sharing reagents and equipment. We thank Justus Kebschull for sharing his insight in MAPseq technique, Maria Doitsidou for sharing her equipment and lab space. We also thank Matt Nolan, Klara Gerlei, Brianna Vandrey, Christina Brown and our lab members for critical reading of the manuscript and Gamze Şener for her help with early experiments. C.M. was supported by a BBSRC project grant BB/M025454/1. This research was supported by a Royal Society and Wellcome Trust Sir Henry Dale fellowship 211236/Z/18/Z.

Contributions

S.Y.T. and M.Ö. equally contributed to the study.

G.S. conceptualised the study, acquired funding and administered the project. G.S. and S.Y.T. performed MAPseq experiments and analysed the data. M.Ö., G.S. and E.S. performed electrophysiology experiments and data analysis. Anatomy and histology experiments were performed and analysed by S.Y.T., G.S., M.Ö., E.S., and M.R.. C.M. developed reagents. Z.B. developed analysis tools and contributed to early discussions. G.S., S.Y.T., E.S. and M.Ö. prepared the original manuscript.

References

Arber, S., Ladle, D.R., Lin, J.H., Frank, E., and Jessell, T.M. (2000). ETS gene Er81 controls the formation of functional connections between group Ia sensory afferents and motor neurons. Cell *101*, 485–498.

Beed, P., de Filippo, R., Holman, C., Johenning, F.W., Leibold, C., Caputi, A., Monyer, H., and Schmitz, D. (2020). Layer 3 Pyramidal Cells in the Medial Entorhinal Cortex Orchestrate Up-Down States and Entrain the Deep Layers Differentially. Cell Rep. *33*, 108470.

Cappaert, N.L.M., Van Strien, N.M., and Witter, M.P. (2015). Chapter 20 - Hippocampal Formation. In The Rat Nervous System (Fourth Edition), G. Paxinos, ed. (San Diego: Academic Press), pp. 511–573.

Colgin, L.L. (2016). Rhythms of the hippocampal network. Nature Reviews Neuroscience *17*, 239–249.

Czajkowski, R., Sugar, J., Zhang, S.-J., Couey, J.J., Ye, J., and Witter, M.P. (2013). Superficially projecting principal neurons in layer V of medial entorhinal cortex in the rat receive excitatory retrosplenial input. J. Neurosci. *33*, 15779–15792.

Dolorfo, C. L., and D. G. Amaral. 1998. Entorhinal Cortex of the Rat: Topographic Organization of the Cells of Origin of the Perforant Path Projection to the Dentate Gyrus. The Journal of Comparative Neurology 398 (1): 25–48.

Dudman, J.T., Tsay, D., and Siegelbaum, S.A. (2007). A role for synaptic inputs at distal dendrites: instructive signals for hippocampal long-term plasticity. Neuron *56*, 866–879.

Frankland, P. W. & Bontempi, B. The organization of recent and remote memories. *Nat. Rev. Neurosci.* **6**, 119–130 (2005).

Gerfen, C.R., Paletzki, R., and Heintz, N. (2013). GENSAT BAC cre-recombinase driver lines to study the functional organization of cerebral cortical and basal ganglia circuits. Neuron *80*, 1368–1383.

Kebschull, J.M., da Silva, P.G., Reid, A.P., Peikon, I.D., Albeanu, D.F., and Zador, A.M. (2016). High-Throughput Mapping of Single-Neuron Projections by Sequencing of Barcoded RNA. Neuron *91*, 975–987.

Khodagholy, D., Gelinas, J.N., and Buzsáki, G. (2017). Learning-enhanced coupling between ripple oscillations in association cortices and hippocampus. Science *358*, 369–372.

Kitamura, T., Pignatelli, M., Suh, J., Kohara, K., Yoshiki, A., Abe, K., and Tonegawa, S. (2014). Island Cells Control Temporal Association Memory. Science *343*, 896–901.

Kitamura, T., Ogawa, S.K., Roy, D.S., Okuyama, T., Morrissey, M.D., Smith, L.M., Redondo, R.L., and Tonegawa, S. (2017). Engrams and circuits crucial for systems consolidation of a memory. Science *356*, 73–78.

Kloosterman, F., Van Haeften, T., Witter, M.P., and Lopes Da Silva, F.H. (2003). Electrophysiological characterization of interlaminar entorhinal connections: an essential link for re-entrance in the hippocampal-entorhinal system. Eur. J. Neurosci. *18*, 3037–3052.

Köhler, C. (1985). A projection from the deep layers of the entorhinal area to the hippocampal formation in the rat brain. Neurosci. Lett. *56*, 13–19.

Koster, R., Chadwick, M.J., Chen, Y., Berron, D., Banino, A., Düzel, E., Hassabis, D., and Kumaran, D. (2018). Big-Loop Recurrence within the Hippocampal System Supports Integration of Information across Episodes. Neuron *99*, 1342–1354.e6.

Kumaran, D., Hassabis, D., and McClelland, J.L. (2016). What Learning Systems do Intelligent Agents Need? Complementary Learning Systems Theory Updated. Trends Cogn. Sci. *20*, 512–534.

Kumaran, D., and McClelland, J.L. (2012). Generalization through the recurrent interaction of episodic memories: a model of the hippocampal system. Psychol. Rev. *119*, 573–616.

Marr, D. (1971). Simple memory: a theory for archicortex. Philos. Trans. R. Soc. Lond. B Biol. Sci. *262*, 23–81.

McClelland, J.L., McNaughton, B.L., and O'Reilly, R.C. (1995). Why there are complementary learning systems in the hippocampus and neocortex: insights from the successes and failures of connectionist models of learning and memory. Psychol. Rev. *102*, 419.

McClure, C., Cole, K.L.H., Wulff, P., Klugmann, M., and Murray, A.J. (2011). Production and titering of recombinant adeno-associated viral vectors. J. Vis. Exp. e3348.

Murray, A.J., Sauer, J.-F., Riedel, G., McClure, C., Ansel, L., Cheyne, L., Bartos, M., Wisden, W., and Wulff, P. (2011). Parvalbumin-positive CA1 interneurons are required for spatial working but not for reference memory. Nat. Neurosci. *14*, 297–299.

Naber, P.A., Lopes da Silva, F.H., and Witter, M.P. (2001). Reciprocal connections between the entorhinal cortex and hippocampal fields CA1 and the subiculum are in register with the projections from CA1 to the subiculum. Hippocampus *11*, 99–104.

Ognjanovski, N., Schaeffer, S., Wu, J., Mofakham, S., Maruyama, D., Zochowski, M., and Aton, S.J. (2017). Parvalbumin-expressing interneurons coordinate hippocampal network dynamics required for memory consolidation. Nat. Commun. *8*, 15039.

Ohara, S., Onodera, M., Simonsen, Ø.W., Yoshino, R., Hioki, H., Iijima, T., Tsutsui, K.-I., and Witter, M.P. (2018). Intrinsic Projections of Layer Vb Neurons to Layers Va, III, and II in the Lateral and Medial Entorhinal Cortex of the Rat. Cell Reports *24*, 107–116.

Ólafsdóttir, H.F., Carpenter, F., and Barry, C. (2016). Coordinated grid and place cell replay during rest. Nat. Neurosci. *19*, 792–794.

Pastoll, H., White, M., and Nolan, M. (2012). Preparation of parasagittal slices for the investigation of dorsal-ventral organization of the rodent medial entorhinal cortex. J. Vis. Exp.

Petreanu, L., Huber, D., Sobczyk, A., and Svoboda, K. (2007). Channelrhodopsin-2–assisted circuit mapping of long-range callosal projections. Nat. Neurosci. *10*, 663–668.

Rozov, A., Rannap, M., Lorenz, F., Nasretdinov, A., Draguhn, A., and Egorov, A.V. (2020). Processing of Hippocampal Network Activity in the Receiver Network of the Medial Entorhinal Cortex Layer V. The Journal of Neuroscience *40*, 8413–8425.

Ruth, R. E., Collier, T. J. & Routtenberg, A. Topography between the entorhinal cortex and the dentate septotemporal axis in rats: I. Medial and intermediate entorhinal projecting cells. J. Comp. Neurol. **209**, 69–78 (1982).

Schapiro, A.C., Turk-Browne, N.B., Botvinick, M.M., and Norman, K.A. (2017). Complementary learning systems within the hippocampus: a neural network modelling approach to reconciling episodic memory with statistical learning. Philos. Trans. R. Soc. Lond. B Biol. Sci. *372*.

Squire, L. R., Genzel, L., Wixted, J. T. & Morris, R. G. Memory consolidation. Cold Spring Harb. Perspect. Biol. **7**, a021766 (2015).

Sürmeli, G., Marcu, D.C., McClure, C., Garden, D.L.F., Pastoll, H., and Nolan, M.F. (2015). Molecularly Defined Circuitry Reveals Input-Output Segregation in Deep Layers of the Medial Entorhinal Cortex. Neuron *88*, 1040–1053.

Swanson, L.W., and Köhler, C. (1986). Anatomical evidence for direct projections from the entorhinal area to the entire cortical mantle in the rat. J. Neurosci. *6*, 3010–3023.

Tamamaki, N., and Nojyo, Y. (1995). Preservation of topography in the connections between the subiculum, field CA1, and the entorhinal cortex in rats. J. Comp. Neurol. *353*, 379–390.

Wang, Y., Kakizaki, T., Sakagami, H., Saito, K., Ebihara, S., Kato, M., Hirabayashi, M., Saito, Y., Furuya, N., and Yanagawa, Y. (2009). Fluorescent labeling of both GABAergic and glycinergic neurons in vesicular GABA transporter (VGAT)–Venus transgenic mouse. Neuroscience *164*, 1031–1043.

Witter, M.P., and Amaral, D.G. (1991). Entorhinal cortex of the monkey: V. Projections to the dentate gyrus, hippocampus, and subicular complex. J. Comp. Neurol. *307*, 437–459.

Witter, M.P., Doan, T.P., Jacobsen, B., Nilssen, E.S., and Ohara, S. (2017). Architecture of the Entorhinal Cortex A Review of Entorhinal Anatomy in Rodents with Some Comparative Notes. Front. Syst. Neurosci. *11*, 46.

Wozny, C., Beed, P., Nitzan, N., Pössnecker, Y., Rost, B.R., and Schmitz, D. (2018). VGLUT2 Functions as a Differential Marker for Hippocampal Output Neurons. Front. Cell. Neurosci. *12*, 337.

Xia, F., Richards, B.A., Tran, M.M., Josselyn, S.A., Takehara-Nishiuchi, K., and Frankland, P.W. (2017). Parvalbumin-positive interneurons mediate neocortical-hippocampal interactions that are necessary for memory consolidation. Elife *6*.

Extended Data Figures

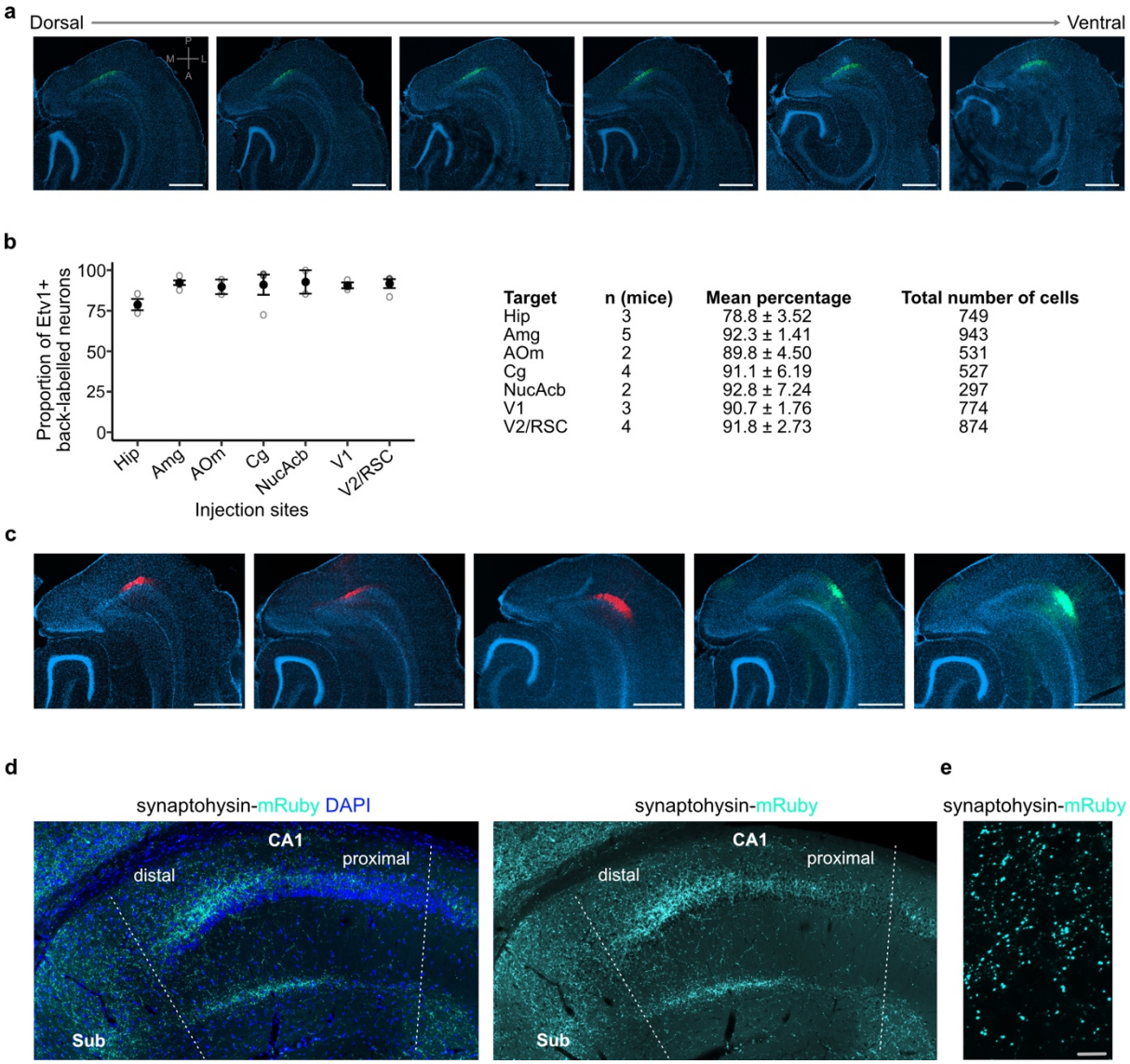

Target	n (mice)	Mean percentage	Total number of cells
Hip	3	78.8 ± 3.52	749
Amg	5	92.3 ± 1.41	943
AOm	2	89.8 ± 4.50	531
Cg	4	91.1 ± 6.19	527
NucAcb	2	92.8 ± 7.24	297
V1	3	90.7 ± 1.76	774
V2/RSC	4	91.8 ± 2.73	874

Extended Data Figure 1. Injection site images, quantification of co-localisation between retrograde markers and Etv1, synaptic terminal imaging in CA1.
a, Horizontal brain sections from a single brain show the dorso-ventral spread of virus-mediated reporter gene expression (Scale bar: 500 µm).
b, Quantification of overlap between retrograde labelling from cortical and subcortical areas and Etv1 expression in L5a of the MEC. The number of mice, mean proportion and total cells counted for each area are shown in the table.
c, Representative injection sites for brains used for quantifying the difference in axon density between proximal and distal CA1 show the medio-lateral extent of injections in the MEC
(Scale bar: 500 µm).
d, Horizontal view of hippocampal CA1 showing axon terminals of entorhinal L5a neurons (cyan).
e, A high contrast high magnification image showing synaptic puncta labelling in stratum pyramidale**.** (Scale bar: 10 µm).
Hip, hippocampus; Amg, amygdala; AOm, medial anterior olfactory area; Cg, cingulate area; NAc, nucleus accumbens; V1, primary visual cortex; V2, secondary visual areas; RSC, retrosplenial cortex.

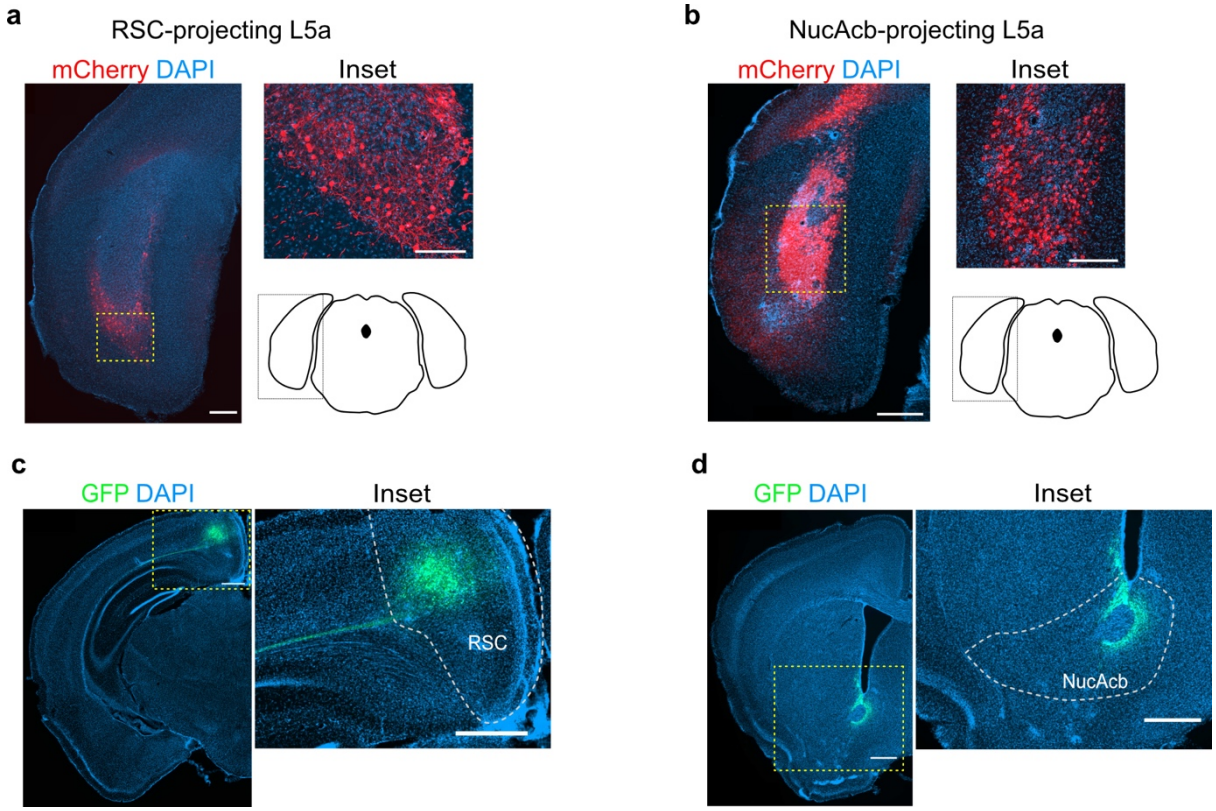

Extended Data Figure 2. Images of injection sites.
a, b, Coronal brain sections showing labelled neurons in MEC with the combinatorial viral strategy (Scale bar: 500 μm). Inset: high-magnification confocal image of boxed region in left panel showing cell bodies in MEC expressing mCherry.
c, d, Coronal brain sections showing GFP expression at the injection sites in retrosplenial cortex (**c**) or nucleus accumbens (**d**) (Scale bar: 500 μm). Inset: high-magnification of boxed region in left panel.

RSC, retrosplenial cortex; NucAcb, nucleus accumbens.

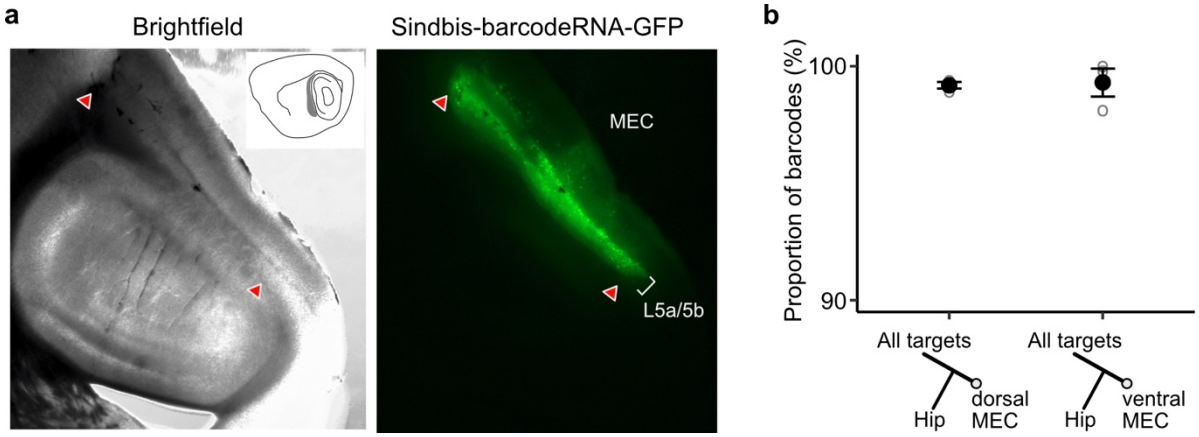

Extended Data Figure 3. Verification of viral expression and further MAPseq data visualisation.
a, Brightfield and epifluorescence microscope images of the injection site on a sagittal brain section showing the spread of neurons infected by the MAPseq virus library.
b, A neuron's position in the dorso-ventral axis does not affect the likelihood of collateralisation of its axons to the hippocampus (Paired two-tailed Wilcoxon signed rank test, $p = 0.75$, median proportion of collateralizing barcodes in dEC = 98.4%, vEC = 98.9%, $n = 3$).

a

	SO (n = 18)	SP Pyr (n = 64)	SP FSint (n = 34)	SP NFSint (n = 15)	SR (n = 14)
Vm rest (mV)	-63 ± 1.48	-66.7 ± 0.6	-63.7 ± 0.7	-63.1 ± 0.9	-60.3 ± 1.3
IR (MΩ)	339 ± 64.1	146.9 ± 6.5	178.2 ± 29.4	214.1 ± 18.3	287.3 ± 48.7
Tm (ms)	22.3 ± 6.8	23.4 ± 2.1	14.7 ± 1.7	21.2 ± 3.7	25.2 ± 4.4
Rheobase (pA)	65.8 ± 17.8	112.8 ± 8.5	128.2 ± 15.1	83.9 ± 12.3	62.8 ± 8.8
Sag coefficient	0.85 ± 0.2	0.85 ± 0.01	0.86 ± 0.02	0.87 ± 0.01	0.85 ± 0.02

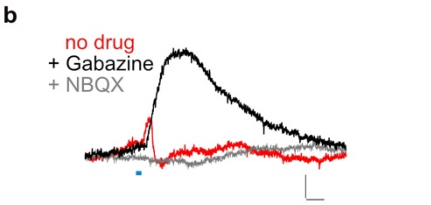

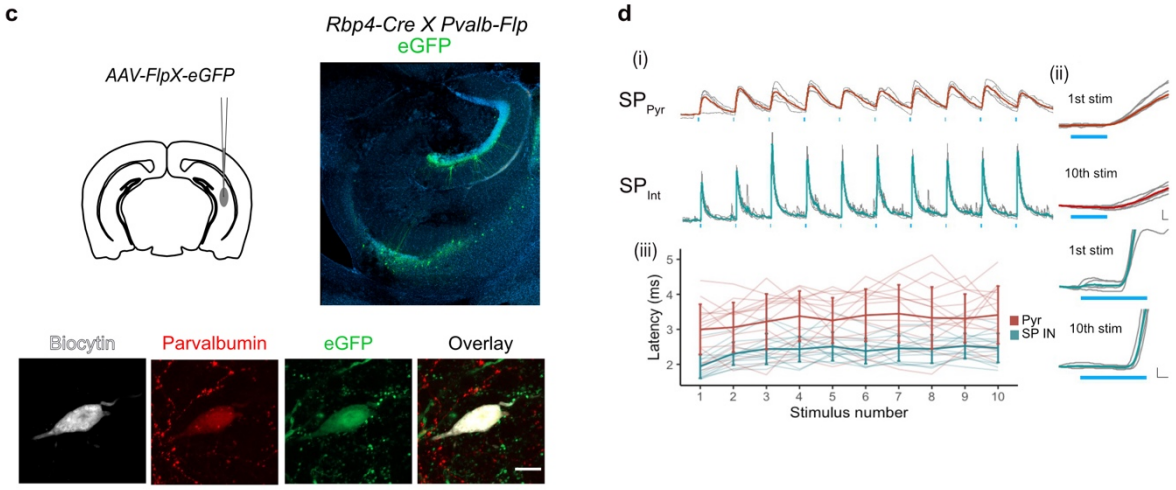

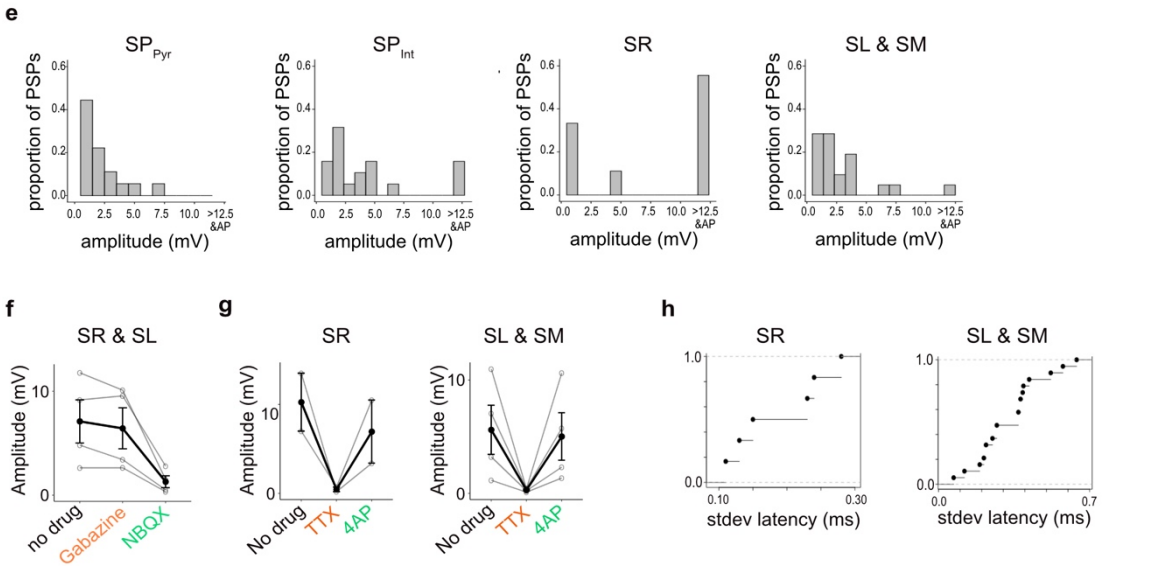

Extended Data Figure 4. Experimental design and properties of responses to optogenetic stimulation

a, Summary table for biophysical properties of neurons recorded in the study.

b, An example of a biphasic response recorded from a pyramidal neuron upon 3ms stimulation of axons of MEC L5a neurons in CA1. A late hyperpolarising (red) response was abolished by application of Gabazine to reveal a larger depolarising PSP (black) which was abolished by application of NBQX (grey) (Scale bar: 10 ms, 0.5 mV).

c, Experimental strategy for fluorescence guided patch-clamp recordings made from Parvalbumin expressing neurons. Left: A FlpX-dependent GFP expressing virus was injected in the hippocampus in *Rbp4-CreX Pvalb-Flp* mice. Right: Confocal image of horizontal slice showing labelled interneurons. Bottom: An example fast-spiking interneuron marked as described in **c**, that showed depolarising PSP upon light stimulation. During recording, the neuron was filled with biocytin and later stained with Streptavidin and Anti-Parvalbumin antibody.

d, (i) Traces of responses to a train of 10 light stimulation (blue lines), showing relatively stable EPSP amplitude across simulations. (Scale bar: 30 ms, 1 mV) (ii) Magnified images of 1st and 10th pulse illustrate the invariant latency in one example cell (Scale bars: 0.5 ms, 0.5 mV) (iii) Quantification of latency across the train in all cells. Error bars represent SEM.

e, Plots showing the frequency distribution of PSP amplitudes in pyramidal neurons and interneurons. PSPs over 12.5 mV were detected in interneurons and often resulted in spiking responses. (SP_{Pyr} : n = 19, SP_{int} : n = 19, SR : n = 9, SL&SM : n = 22 cells).

f, Effects of bath application of Gabazine and NBQX on PSPs recorded from interneurons in SR and SL. The PSP amplitudes were largely unaffected by application of Gabazine (SR: n = 2 cells & SL n = 2 cells, p = 0.28, 2-tailed Student's t test) but were largely blocked by NBQX (SR: n = 2 cells & SL n = 2 cells, p = 0.04, 2-tailed Student's t test) indicating AMPA receptor mediated glutamatergic synaptic transmission.
g, Effects of bath application of TTX and 4-AP on the response amplitude PSPs recorded from interneurons in SR, SL and SM (SR: n = 2, SL: n = 3, SM: n = 1 cells).
h, Cumulative probability plots of standard deviation of latencies for neurons with PSP responses that were > 1 mV in amplitude. EPSPs of interneurons in all layers except SO had a short latency after light stimulation (mean latency SR: 2.00 ± 0.08 ms, n = 6 cells; SL & SM: 2.12 ± 0.21 ms, n = 23 cells). In SO 2 out of 3 of the evoked PSPs had a larger latency of onset (mean latency = 8.5 ± 0.63 ms, n = 2 cells, 2 mice, data not shown).